

Landscape-induced spatial oscillations in population dynamics

Vivian Dornelas ¹, Eduardo H. Colombo ², Cristóbal López ², Emilio Hernández-García ², and Celia Anteneodo ^{1 3}

¹ *Department of Physics, PUC-Rio, Rua Marquês de São Vicente, 225, 22451-900, Rio de Janeiro, Brazil.*

² *IFISC (CSIC-UIB), Campus Universitat Illes Balears, 07122, Palma de Mallorca, Spain.*

³ *Institute of Science and Technology for Complex Systems, Rio de Janeiro, Brazil.*

Abstract

We study the effect that disturbances in the ecological landscape exert on the spatial distribution of a population that evolves according to the nonlocal FKPP equation. Using both numerical and analytical techniques, we explore the three types of stationary profiles that can develop near abrupt spatial variations in the environmental conditions vital for population growth: sustained oscillations, decaying oscillations and exponential relaxation towards a flat profile. We relate the wavelength and decay length of the wrinkles to the shape of the interaction kernel. Since these spatial structures encode details about the interaction among individuals, we discuss how heterogeneities reveal information that would be hidden in a flat landscape.

1. Introduction

The Fisher-Kolmogorov-Petrovskii-Piskunov (FKPP) equation [1, 2, 3] is the standard model describing, at a continuum level, the spatio-temporal dynamics of a population of individuals that diffuse, grow and compete for resources. In one dimension, it is given by

$$\partial_t \rho(x, t) = D \partial_{xx} \rho(x, t) + a \rho(x, t) - b \rho^2(x, t), \quad (1)$$

where $\rho(x, t)$ is the population density at position x and time t , D is the diffusion coefficient, a is the (clonal) reproduction rate, and b is the strength of (intraspecific) competition that bounds population growth. In Eq. (1)

competition is local in the sense that it occurs at scales much shorter than those associated to the diffusion process. However, competition effects might also extend to larger scales, making the interaction essentially nonlocal [4, 5, 6]. For instance, nonlocal cooperation and competition can be present in vegetation mediated by roots [7, 8, 9]. Also, nonlocality can emerge due to the spread of substances released or consumed by the individuals [7, 10, 11, 12]. Then, assuming that competition can act at a distance according to an interaction kernel (also called influence function) γ , Eq. (1) is extended as

$$\partial_t \rho(x, t) = D \partial_{xx} \rho(x, t) + a \rho(x, t) - b \rho(x, t) [\gamma \star \rho](x, t), \quad (2)$$

where $[\gamma \star \rho](x, t) \equiv \int_{-\infty}^{\infty} \gamma(x - x') \rho(x', t) dx'$, and $\int_{-\infty}^{\infty} \gamma(x) dx = 1$. Differently from the original FKPP Eq. (1), the nonlocal FKPP equation, given by Eq. (2), can exhibit self-organized structures depending primarily on the particular properties of the kernel and secondarily on the values of the diffusion and reproduction rates [5, 6, 13, 14]. Moreover, Eq. (2) assumes a homogeneous environment, which is implicit in the constant coefficients. But, actually, in biological systems, environmental factors suffer spatial variations [15, 16, 17]. In this paper, we exploit that they can stress the system and resonate with the internal scales, generating spatial oscillations in the distribution of the population [18, 4, 19]. In order to do that, we consider the following extension of Eq. (2),

$$\partial_t \rho(x, t) = D \partial_{xx} \rho(x, t) + \Psi(x) \rho(x, t) - b \rho(x, t) [\gamma \star \rho](x, t), \quad (3)$$

where the spatially-dependent reproduction rate $\Psi(x)$ reflects the overall habitat quality at a given location x [17].

Previous studies have considered different forms for Ψ , accounting for diverse complex spatiotemporal features of natural environments [18, 20, 19, 4]. In this work, we focus on sharp spatial changes in the environmental conditions relevant for the population under consideration [17, 16, 21]. This kind of change is found in diverse situations in nature, e.g., at the interface between forest and grassland [17], at the bounds of oases [15] or harmful regions [8], or in artificial lab experiments [16], where there is a neat contrast of spatial domains with different growth rates. Contemplating these cases justifies attributing the Heaviside step or rectangular functions to $\Psi(x)$. We will see that three kinds of stationary (long time) population profiles can develop from the interface: *sustained oscillations* (or spatial patterns, without amplitude decay), *decaying oscillations* (with decreasing amplitude from the

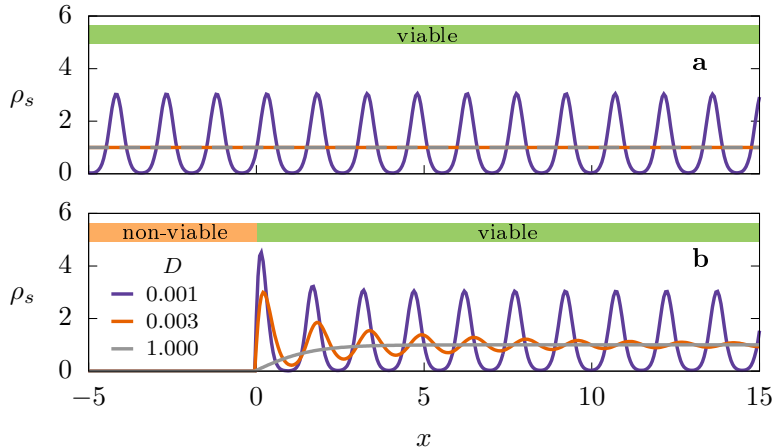


Figure 1: **Population distribution in a medium which is (a) homogeneously viable, (b) heterogeneous, with viable and non-viable regions.** Depending on the values of the parameters in Eq. (3), spatial patterns can develop around the uniform steady state in (a), and they are preserved in the viable region of the corresponding case in (b). But even when the steady state is uniform in case (a), decaying oscillations can emerge in (b). Parameters are $a = b = 1$, values of D are given in the legend, and for kernel γ_q defined in Eq. (4), we fix $q = -0.5$ and $\ell = 2$. For panel b, A in Eq. (9) is $A \rightarrow \infty$.

interface) or *exponential decay* towards a flat profile. These behaviors are schematically depicted in Fig. 1 and will be discussed quantitatively later.

Following computational and theoretical approaches, we have investigated the conditions for the emergence of the different steady regimes. It is interesting to note that the interface acts as a lens revealing structures that would be hidden in a flat landscape, as depicted in Fig. 1. We will also discuss how these structures are associated with the internal scales, providing information on the interaction kernel.

The paper is organized as follows. In Sec. *Preliminaries*, we provide introductory information with general considerations about the homogeneous environment as a frame of reference. In Sec. *Heterogeneous landscapes*, we present the main results for 1D landscapes with sharp changes, derived from numerical integration of Eq. (3) as well as from a theoretical framework. Then, we discuss how information about the interaction kernel can be extracted from observable oscillations. Additionally, outcomes for 2D land-

scapes are shown to illustrate that the main phenomenology investigated is not restricted to 1D. A summary of the main findings and concluding remarks are presented in Sec. *Discussion and concluding remarks*.

2. Preliminaries

In this section, we first define the main class of influence functions that will be used in numerical examples throughout the paper. We also revisit the linear response analysis for the homogeneous environment, which serves as a reference frame for the more complex heterogeneous case.

2.1. Interaction kernel

We have chosen a family of influence functions that allows us to continuously vary its compactness:

$$\gamma_q(x) = N_q[1 - (1 - q)|x|/\ell]_+^{1/(1-q)} \equiv N_q \exp_q(|x|/\ell), \quad (4)$$

where q and ℓ control the shape of the kernel and N_q is a normalization constant. The subindex $+$ means $[z]_+ = 0$ if $z \leq 0$. This kernel is based on a generalization of the exponential function, known as q -exponential [22]. In the limit $q \rightarrow 1$, the standard exponential is approached yielding $\gamma_1(x) \propto e^{-|x|/\ell}$. The kernel shapes are illustrated in Fig. 2a. As we will see, it is specially relevant the fact that, only for $q < 0$, the Fourier transform of $\gamma_q(x)$ can take negative values. Then, we focus on the range $-1 \leq q < 1$, around this critical value. Moreover, in this range, the interaction is restricted to a finite region and the kernel moments are well-defined, fact that will facilitate both the numerical and theoretical approaches. The family of stretched exponential kernels was also considered for comparison (see Appendix).

2.2. Homogeneous landscapes

For a homogeneous landscape, $\Psi(x) = a$, the linearization of Eq. (3), around its uniform solution $\rho_0 = a/b$, by setting $\rho(x, t) = \rho_0 + \varepsilon(x, t)$ (with $\varepsilon/\rho_0 \ll 1$) gives, in Fourier space, $\partial_t \tilde{\varepsilon}(k, t) = [-Dk^2 - a\tilde{\gamma}(k)]\tilde{\varepsilon}(k, t)$, where $\tilde{\gamma}(k) = \int_{-\infty}^{\infty} \gamma(x)e^{-ikx} dx$ is the Fourier transform of the interaction kernel γ . The factor between square brackets represents the mode growth rate

$$\lambda(k) = -Dk^2 - a\tilde{\gamma}(k), \quad (5)$$

whose shape is plotted in Fig. 2b, for each kernel γ_q shown in Fig. 2a. It is the important quantity that will appear all throughout the paper. In terms

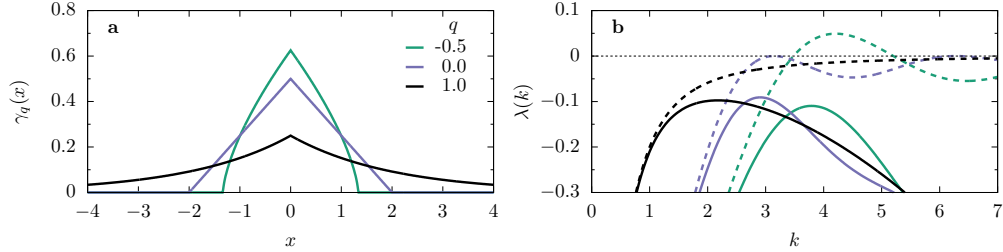


Figure 2: **Interaction kernel and mode stability in a homogeneous medium.** (a) $\gamma_q(x)$, defined in Eq. (4), for the values of q indicated on the figure, and $\ell = 2$. (b) Mode growth rate $\lambda(k)$ given by Eq. (5), for $a = b = 1$, with $D = 0$ (dashed lines) and $D = 0.01$ (solid lines), corresponding to the values of q plotted in (a). The case $q = 0$ (triangular kernel) is the critical one, for which the maximal value of $\lambda(k)$ at finite k is zero when $D = 0$. Notice that, when diffusion is absent, the mode growth rate is proportional to the kernel Fourier transform.

of it, $\tilde{\varepsilon}(k, t) = \tilde{\varepsilon}(k, 0)e^{\lambda(k)t}$. Thus, if $\lambda < 0$, any initial perturbation will fade out, such that in the long-time limit the population distribution $\rho(x)$ will be flat. On the contrary, if there are unstable modes, with $\lambda(k) > 0$, stationary sustained oscillations will be produced with a characteristic mode k^* (the maximum of λ), which is the initially fastest growing one [23].

From Eq. (5), $\lambda(k) > 0$ occurs for sufficiently small D if the Fourier transform of the kernel takes some negative values. Then, by substitution of $\tilde{\gamma}_q$ into Eq. (5), we conclude that sustained oscillations can only appear if $\gamma_q(x)$ is sub-triangular, i.e., $q < 0$ (in the critical case $q = 0$, $\gamma_q(x)$ produces the triangular kernel, whose Fourier transform is $\tilde{\gamma}_0(k) = \sin^2(k\ell)/(k\ell)^2$). This is a necessary but not sufficient condition that arises by imposing $\lambda(k^*) > 0$ in the most favorable case $D = 0$ (hence $\tilde{\gamma}(k^*) < 0$), to induce the growth of certain modes. In contrast, for $q \geq 0$, the uniform state is intrinsically stable (that is, independently of the remaining parameters). In Fig. 2b, we plot the mode growth rate for $D = 0$ and $D > 0$, which shows how diffusion affects mode stability, damping fluctuations.

Concerning the interaction length $\ell > 0$, when $D = 0$, it simply scales the wavenumber as $k\ell$. Therefore, when ℓ goes to zero (implying local dynamics), the dominant wavenumber k^* is shifted to infinity, meaning that patterns go continuously to a flat profile in that limit. In contrast, for $D > 0$, the first term in Eq. (5) has a more homogenizing effect the larger k^* , hence

the smaller ℓ . As a consequence, there is a critical value of ℓ below which patterns do not emerge, even if for finite ℓ there is nonlocality [23]. Finally, there is also a critical value a_c of the reproduction rate, when $D > 0$, and with all the other parameters fixed, such that sustained oscillations emerge only for $a > a_c$.

In summary, in the cases where $\lambda(k^*) \leq 0$ (i.e., either $q \geq 0$, or alternatives involving $q < 0$ such as large enough D , small enough ℓ) or small enough a , information regarding the interaction scale ℓ or other details of the kernel profile are not stamped in the spatial distribution $\rho(x, t)$, which becomes uniform at long times.

3. Heterogeneous landscapes

In this section, the heterogeneity of the landscape is introduced by assuming that its profile can be written as $\Psi(x) = a + \psi(x)$, where $\psi(x)$ represents the spatial variations of the environment around a reference level a .

The results that we will present were obtained through theoretical and numerical techniques. The theoretical approach is based on mode linear stability analysis discussed in the previous section. In parallel, we will show results obtained by numerically solving Eq. (3). Numerical integration was performed starting from a locally homogeneous state (that is homogeneous in each region where the growth rate is constant) plus a very small amplitude uniformly distributed random perturbation, following a standard forward-time-centered-space scheme which is fourth-order Runge-Kutta in time and second-order in space, with spatial and temporal discretization $\Delta x = 0.05$ and $\Delta t \in [10^{-2}, 10^{-4}]$ (depending on D), respectively.

3.1. Refuge

As paradigm of a heterogeneous environment with sharp borders, we first consider that the spatial variations around the reference level a are given by

$$\psi(x) = -A[1 - \Theta(L/2 - |x|)], \quad (6)$$

where Θ is the Heaviside step function. With $A > 0$, it represents a refuge of size L with growth rate a immersed in a less viable environment with growth rate $a - A$. In a laboratory situation, this can be constructed by means of a mask delimiting a region that protects organisms from some harmful agent, for instance, shielding bacteria from UV radiation [16]. In natural

environments, this type of localized disturbance appears due to changes in the geographical and local climate conditions[17], or even engineered by other species [8].

In Sec. *Homogeneous landscapes*, we have seen that the uniform distribution is intrinsically stable when $q \geq 0$. In contrast, even if for $q \geq 0$, spatial structures can emerge due to heterogeneities in $\Psi(x)$, as illustrated in Fig. 3 for the case $D = 0.01$.

In the limit of weak heterogeneity, i.e., under the condition $|\psi(x)|/a \ll 1$, we obtain an approximate analytical solution assuming that the steady solution of Eq. (3) can be expressed in terms of a small deviation $\varepsilon_s(x)$ around the homogeneous state $\rho_0 = a/b$. Then, we substitute $\rho_s(x) = \rho_0 + \varepsilon_s(x)$ into the stationary form of Eq. (3), discard terms of order equal or higher than $\mathcal{O}(\varepsilon^2, A\varepsilon, A^2)$, and Fourier transform, obtaining

$$\tilde{\varepsilon}_s(k) = \frac{\rho_0 \tilde{\psi}(k)}{-\lambda(k)}, \quad (7)$$

where $\lambda(k)$ was already defined in Eq. (5) and $\tilde{\psi}(k)$ is the Fourier transform of the small fluctuations in the landscape quality, which for the case of Eq. (6) is $\tilde{\psi}(k) = A[2 \sin(Lk/2)/k - 2\pi\delta(k)]$.

Finally, assuming that $\lambda(k^*) < 0$, the steady density distribution is given by

$$\rho_s(x) = \rho_0 + \varepsilon_s(x) = \rho_0 + \mathcal{F}^{-1} \left(\frac{\rho_0 \tilde{\psi}(k)}{-\lambda(k)} \right), \quad (8)$$

where the inverse Fourier transform \mathcal{F}^{-1} must be numerically computed in general. For small heterogeneity, Eq. (8) is in very good agreement with the exact numerical solution obtained by integration of the dynamics Eq. (3), as can be seen in Fig. 3. Notice the two different profiles, depending on the diffusion coefficient D : one gently following the landscape heterogeneity and the other strongly oscillatory.

For small D , the induced oscillations display two evident characteristics, which depend on $\tilde{\gamma}_q$: well-defined wavenumber and decaying amplitude for increasing distances from the interfaces at $x = \pm L/2$ (highlighted by dashed vertical lines in Fig. 3). We will see that the details of the kernel γ_q can be seen in through the characteristics of the oscillations.

3.2. *Semi-infinite habitat*

Since oscillations are induced by changes in the landscape, it is worth focusing, from now on, on one of the interfaces. Moreover, we assume a refuge

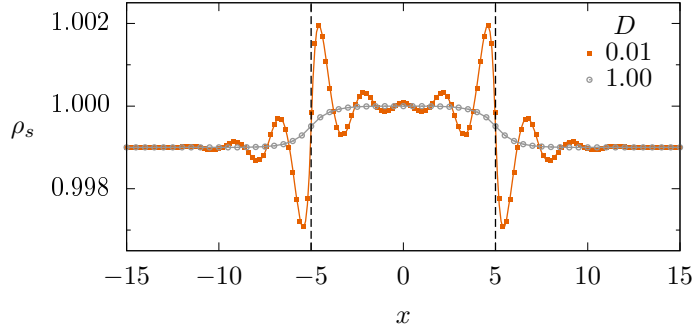


Figure 3: **Stationary population density ρ_s vs. x in a refuge.** This heterogeneous environment is defined by Eq. (6), with $a = b = 1$, $A = 10^{-3}$ and $L = 10$. The vertical lines indicate the refuge boundaries. We used the kernel $\gamma_q(x)$, with $q = 0.1$ and $\ell = 2$, and two different values of D . Symbols are results from numerical integration of Eq. (3), and solid lines from the small- A approximation given by Eq. (8), in excellent agreement with the exact numerical solution. Recall that, in a homogeneous environment, no oscillation appear for $q \geq 0$.

much larger than the oscillations wavelength, sufficient to follow over several cycles the structure originated at the interface. To do that, we consider a semi-infinite habitat defined by

$$\psi(x) = -A\Theta(-x), \quad (9)$$

where for convenience the interface was shifted to $x = 0$, such that the low-quality region is at $x < 0$. As an additional feature, we consider that the harmful conditions are very strong, that is, $A \rightarrow \infty$. The purpose is twofold, on the one hand it allows to test the robustness of the results beyond the small- A approximation, on the other it allows a simplification as follows. When $A \gg a$, ρ is very small in the unfavorable region, then the nonlinear competition term in Eq. (3) can be neglected, leading to a steady distribution that decays exponentially from the interface as $\rho(x < 0) \sim \exp[\sqrt{(A-a)/D}x]$. Thus, in the limit $A \rightarrow \infty$, we have $\rho(x \leq 0, t) = 0$. This is the setting used to produce Fig. 1b, by numerical integration of Eq. (3).

As sketched in Fig. 4, for each steady distribution attained at long times, we measure the wavelength, from which we obtain the wavenumber \bar{k} , and

the decay length \bar{x} , by observing that the envelope of the oscillations decays as $\exp(-x/\bar{x})$.

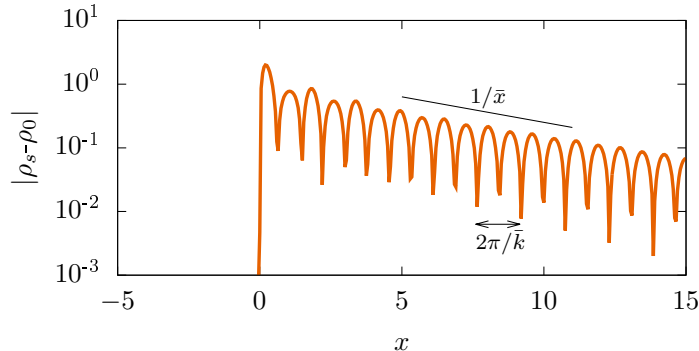


Figure 4: **Characterization of stationary profiles.** (a) Long-time solutions approach a stationary state characterized by the wavelength $2\pi/\bar{k}$ and decay length \bar{x} . This example was obtained from numerical integration of Eq. (3), assuming a semi-infinite habitat, with parameters $D = 0.003$, $\gamma_q(x)$ with $\ell = 2$ and $q = -0.5$.

The stationary spatial structures that emerge for $x > 0$ can be classified into the three types depicted in Fig. 1: *sustained oscillations* (lilac line, with $\bar{k} > 0$ and $\bar{x} \rightarrow \infty$); *decaying oscillations* (orange line, with $\bar{k} > 0$ and finite \bar{x}); *exponential decay* (gray line $\bar{k} = 0$ and finite \bar{x}). In the case of Fig. 1b, these three types appear when D changes. We also systematically varied the shape parameter q to construct the phase diagram in the plane $q - D$ presented in Fig. 5a.

To perform a theoretical prediction of \bar{k} and \bar{x} , within the linear approximation, we consider that these oscillation parameters should be related to the poles of the integrand $e^{ikx}\tilde{\psi}(k)/[-\lambda(k)]$ in the expression for the inverse Fourier transform that provides the solution, according to Eq. (8). As far as the external field $\psi(x)$ does not introduce non-trivial poles, like in the case of a Heaviside step function ($\tilde{\psi}(k) \sim 1/k$), only the complex zeros of $\lambda(k)$ matter. The dominant (more slowly decaying mode) is given by the pole $k_r + ik_i$ with minimal positive imaginary part, that except for amplitude and phase constants, will provide approximately patterns of the form $e^{-k_i x} \cos(k_r x)$, allowing the identifications $\bar{k} = k_r$ and $1/\bar{x} = k_i$. This calculation [24] is in very good agreement with the results of numerical simulations presented in Fig. 5, explaining the observed regimes. In fact, the modes

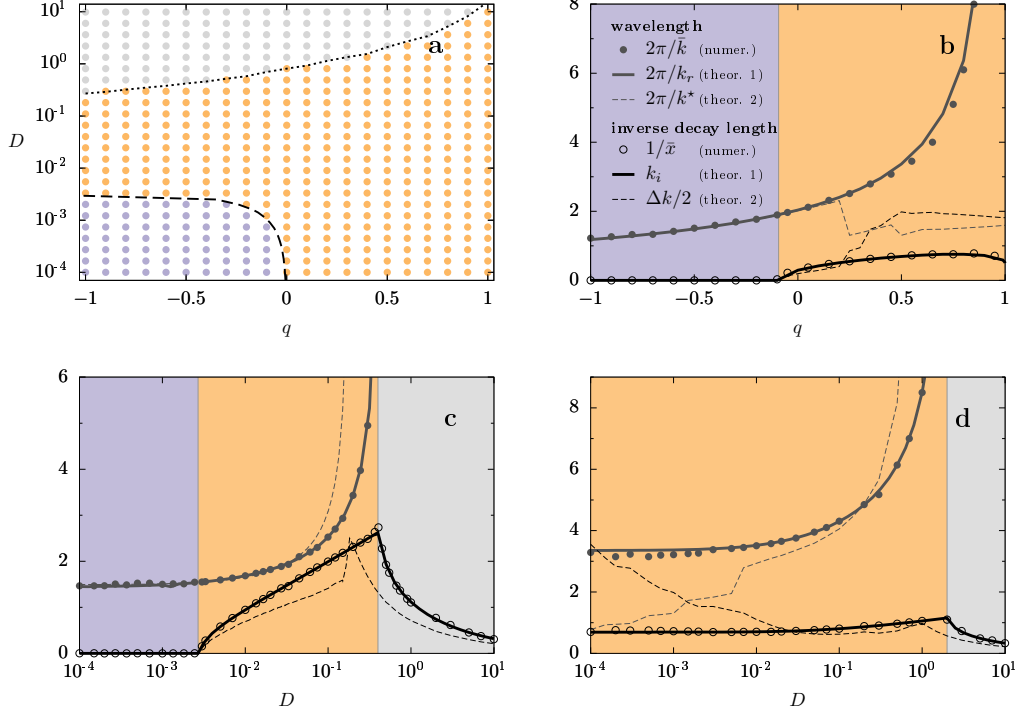


Figure 5: **Phase diagram and characteristics of the stationary profiles as a function of diffusion coefficient D and q , in the semi-infinite habitat.** We used the kernel $\gamma_q(x)$, with $\ell = 2$. (a) Phase diagram in the q – D plane, and cuts at (b) $D = 10^{-3}$, (c) $q = -0.5$ (d) $q = 0.5$. The remaining parameters are $a = b = 1$. In diagram (a), for each point in the grid, the type of regime was determined based on the values of $2\pi/\bar{k}$ and \bar{x} that characterize the solutions of Eq. (3): *sustained oscillations* ($\bar{k} > 0$ and $\bar{x} \rightarrow \infty$, lilac), *decaying oscillations* ($\bar{k} > 0$ and finite \bar{x} , orange), and *pure exponential decay* ($\bar{k} = 0$ and finite \bar{x} , gray). The lines between regimes were determined from $k = k_r + ik_i$, the complex pole with smallest positive imaginary part (dashed line for $k_i = 0$ and dotted line for $k_r = 0$). Its components were also used to determine the full-lines (theoretical 1) in panels (b)–(d). Symbols correspond to measurements of numerical profiles and thin dashed lines to the harmonic estimate (theoretical 2) given by Eq. (13).

that persist beyond the interface have relatively small amplitudes, so that the system response is approximately linear in this region. Recall that this analysis assumes mode stability ($\lambda(k) < 0$). When $\lambda(k^*) > 0$, the system is intrinsically unstable, with the poles having null imaginary part (lying on the real axis). Nevertheless, the initially fastest growing mode, given by the

maximum of $\lambda(k)$, tends to remain the dominant one in the long term [23], yielding $\bar{k} \simeq k^*$ for the sustained oscillations ($\bar{x} \rightarrow \infty$).

Alternatively, to obtain further insights, it is useful to consider the response function $\tilde{R}(k)$ that, from Eq. (7), is

$$\tilde{R}(k) \equiv \frac{|\tilde{\varepsilon}_s(k)|^2}{|\tilde{\psi}(k)|^2} = \frac{\rho_0^2}{\lambda^2(k)}. \quad (10)$$

Moreover, despite it misses some information on the dynamics (contained in the phase of $\lambda(k)$), it can provide a more direct estimation of the observed parameters than through poles calculations. In order to do that, we resort to the bell-shaped response of a forced linear oscillator

$$\tilde{R}_H(k) \equiv \frac{1}{|\lambda_H(k)|^2} = \frac{1}{(k^2 - k_0^2)^2 + 4\zeta^2 k_0^2 k^2}, \quad (11)$$

with $-\lambda_H(k) = -k^2 + i2\zeta k_0 k + k_0^2$, whose zeros (poles of $1/\lambda_H(k)$) are $k = \pm k_r + ik_i = k_0(\pm\sqrt{1 - \zeta^2} + i\zeta)$, where k_0 the natural mode and ζ is the damping coefficient. Note that, under a step forcing $f(x) = k_0^2\Theta(x)$, which simulates our present setting, those poles carry the essential information of the damped-oscillation solution, given by $\tilde{\varepsilon}_H(k) = \tilde{f}(k)/[-\lambda_H(k)]$. In underdamped case ($\zeta < 1$), this solution is explicitly given by

$$\varepsilon_H(x) = \left[1 - \frac{k_0}{\kappa} e^{-x/\xi} \sin(\kappa x + \phi) \right] \Theta(x), \quad (12)$$

where $\kappa = k_0\sqrt{1 - \zeta^2}$ ($= k_r$), $\xi = 1/(\zeta k_0)$ ($= 1/k_i$), and the phase constant $\phi = \tan^{-1}(\xi\kappa)$. The solution for the overdamped case emerges for $\zeta > 1$, when the zeros of $\lambda(k)$ are pure imaginary with $k_i = k_0(\zeta \pm \sqrt{\zeta^2 - 1})$. The connection between the poles of $\tilde{R}_H(k)$ and the dynamic solution is possible because, as previously discussed, \tilde{f} does not introduce relevant poles, and the forced solution has a form similar to the homogeneous one.

The harmonic model is in fact the minimal model for the observed structures and the correspondence between Eqs. (11) and (12) will allow to estimate the oscillation features. In the limit of small ζ , $\tilde{R}_H(k)$ has a sharp peak, characterized by a large quality factor $Q \equiv k^*/\Delta k$, where Δk is the bandwidth at half-height of $\tilde{R}(k)$ around k^* [25]. First, we see that the position of the peak of \tilde{R}_H approximately gives the oscillation mode κ , according to $k^* = k_0\sqrt{1 - 2\zeta^2} = \kappa + \mathcal{O}(\zeta^2)$. Second, the bandwidth is related to the decay-length through $\Delta k = 2/\bar{x} + \mathcal{O}(\zeta^2)$ [26].

Putting all together, as long as $\tilde{R}(k)$ resembles the bell-shaped form of $\tilde{R}_H(k)$, we can use, at first order in ζ , the estimates

$$\bar{k} \simeq \arg \max_k (\tilde{R}) \equiv k^* \quad \text{and} \quad \bar{x} \simeq \frac{2}{\Delta k}. \quad (13)$$

The expression for \bar{x} is also valid in the overdamped limit of large ζ , in which case the maximum is located at $k^* = 0$.

The adequacy of the harmonic framework is illustrated in Fig. 6. In the case $D = 2 \times 10^{-1}$, the harmonic response is able to emulate $\tilde{R}(k)$. Then, if the linear approximation holds, one expects that the estimates given by Eq. (13) should work. In fact, they do work in this case, as we will see below. Differently, when $D = 2 \times 10^{-4}$, $\tilde{R}(k)$ does not follow the harmonic shape, and the prediction of the decay length fails.

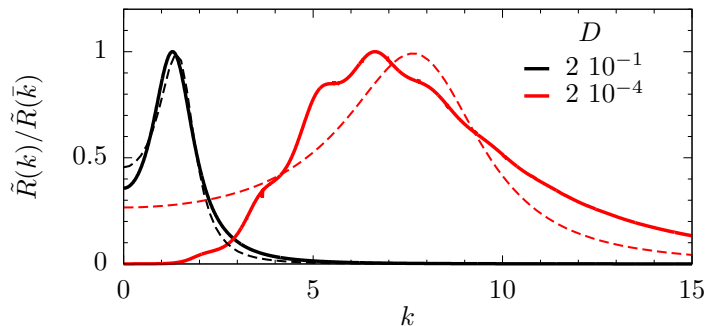


Figure 6: **Comparison of $\tilde{R}(k)$ with the harmonic response $\tilde{R}_H(k)$.** $\tilde{R}(k)$ of our model, given by Eq. (10) (solid lines) and harmonic response $R_H(k)$, given by Eq. (11) (dashed lines), where the values of k_0 and ζ were obtained by fitting Eq. (11) to $\tilde{R}(k)$. In all cases, $q = 0.5$, $\ell = 2$ and two different values of D shown in the legend were considered. Notice that for $D = 2 \times 10^{-1}$, the response can be described by the harmonic approximation. For $D = 2 \times 10^{-4}$, the response is multi-peaked, the harmonic approximation fails and also the dominant mode observed is not given by the absolute maximum, but by the small hump at $k \simeq 2.1$, indicating nonlinear effects.

In Fig. 5, we compare the values of \bar{k} and \bar{x} extracted from the numerical solutions of Eq. (3) with those estimated by Eq. (13) (dashed lines) and, more accurately, with those predicted from the poles of $\tilde{R}(k)$ (solid lines), which perfectly follow the numerical results. The harmonic estimates are shown in the full abscissa ranges, as a reference, even in regions where the

approximation is not expected to hold, because discrepancies give an idea of the departure from the harmonic or linear responses.

Figure 5c shows outcomes for a fixed $q < 0$ ($q = -0.5$), corresponding to a vertical cut in the diagram of Fig. 5a. Sustained oscillations (i.e., $\bar{x} \rightarrow 0$) can emerge for $q < 0$, when diffusion is weak, namely, for $D < D_c \simeq 0.0025$ (lilac colored region), where D_c is obtained from $\lambda(k^*) = 0$. When D increases beyond this critical value, oscillations are damped with a finite characteristic length \bar{x} . For even larger values of D , oscillations completely disappear ($\bar{k} \rightarrow 0$). Note that the comparison between numerics and theory (symbols vs. lines) is good close to the pattern transition point D_c , where the response peak is sharp (large Q). Despite the lack of agreement for larger D , the theoretical prediction qualitatively works with a shift of transition to exponential decay (dotted line).

Figure 5d (which corresponds to vertical cut at $q = 0.5$ in the diagram of Fig. 5a) shows the corresponding results for a fixed $q > 0$ ($q = 0.5$), which is characterized by the absence of sustained patterns. Above $D \simeq 0.02$, the response $\tilde{R}(k)$ is unimodal, a bell-shaped curve that resembles the harmonic response, as shown in Fig. 6, producing a good agreement between theory and numerical results, despite being far from the large- Q limit. However, for smaller values of D , the profile is multi-peaked, compromising the use of the harmonic approximation. Besides that, the observed mode is wrongly predicted by k^* , suggesting strong nonlinear effects. Even so, it is interesting that a detailed analysis of the response function still allows to extract the effective dominant mode, given by the position of its first small hump at $k \simeq 2.1$ representing a ghost dominant mode.

Figure 5b displays \bar{k} and \bar{x} as a function of q , for a fixed value of the diffusion coefficient ($D = 10^{-3}$), corresponding to a horizontal cut in Fig. 5a. Recall that, the smaller the value of q , the more confined is the interaction (thus, the larger is \bar{x}). For $q < q_c \approx -0.093$ there are sustained oscillations ($\bar{x} \rightarrow \infty$). Above q_c , oscillations decay, which is indicated by the transition of $1/\bar{x}$ from null to finite values. Again, near this transition, the linear response prediction is good, but, far from the critical point, nonlinear effects become relevant, as noticed above $q \simeq 0.2$, where there is a strong mismatch between the main mode of the linear response analysis and the numerical one. Also in this case, a small hump in the response function represents the dominant mode.

3.3. Inferring information about the interactions

In this section, we extend the discussion about the mapping between kernel and oscillation parameters, showing how hidden information about the interactions can be extracted from landscape-induced oscillations.

In Sec. *Semi-infinite habitat*, we have shown how the interaction kernel γ_q determines the dominant wavelength \bar{k} and the decay length \bar{x} . Now we aim to show how, reciprocally, information about the interaction kernel can be extracted from the induced oscillations, assuming that the population dynamics is governed by Eq. (3) with unknown kernel γ .

Using the theoretical estimates given by Eq. (13), within their validity range, we plot in Fig. 7a the contour lines for certain wavelengths \bar{k} and decay lengths \bar{x} : $\bar{k}(\ell, q) = \text{constant}$, and $\bar{x}(\ell, q) = \text{constant}$. These contour lines depend both on ℓ and q . However, since \bar{k} is strongly controlled by ℓ , while \bar{x} is more closely related to the shape parameter q , there is crossing of the lines that identify the kernel properties.

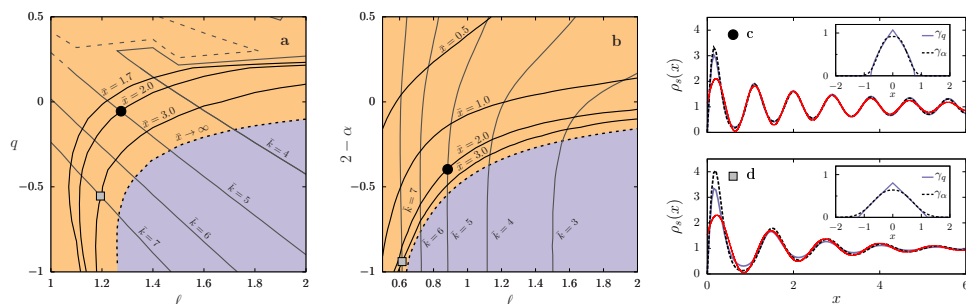


Figure 7: **Determination of oscillation wave number, \bar{k} , and decay length, \bar{x} .** Contour lines for fixed wavelengths and decay lengths. Colors for different oscillatory regimes as in previous figures. We considered interaction following kernel γ_q , given by Eq. (4), in (a) and $\gamma_\alpha \equiv N_\alpha^{-1} e^{-|x/\ell|^\alpha}$ in (b). The remaining parameters are $D = 10^{-3}$ and $a = b = 1$. Two points are highlighted: $(\bar{k}, \bar{x}) = (7, 3)$ (black circle) and $(5, 2)$ (gray square). (c)-(d) Oscillations produced by the kernels shown in the respective insets. The kernels γ_q (solid blue) and γ_α (dashed black) were obtained from oscillation's parameters for the highlighted points. The respective values of the kernel parameters are: (c) $(\ell, q) = (1.19, -0.55)$, $(\ell, \alpha) = (0.61, 2.94)$ (black circle), and (d) $(\ell, q) = (1.275, -0.055)$, $(\ell, \alpha) = (0.883, 2.397)$ (gray square). The red line shows a fit with mode \bar{k} and decay \bar{x} , namely $\rho_H(x) = 1 + B e^{-x/\bar{x}} \sin(\bar{k}x + \phi)$, where B and ϕ were adjusted.

For comparison, we consider in Fig. 7b, the stretched-exponential kernel $\gamma_\alpha(x) \equiv N_\alpha^{-1} \exp(-|x/\ell|^\alpha)$, where N_α is the normalization factor. Additional

results using this kernel can be found in Appendix. Likewise γ_q , which only produces sustained oscillations for $q < 0$ (sub-triangular), the kernel γ_α has the condition $\alpha > \alpha_c = 2$ (platykurtic) [14].

Let us imagine that oscillations with specific values of \bar{k} and \bar{x} are observed (black circles and gray squares in Fig. 7)c-d. Then, assuming a particular kernel, we can extract the interaction length ℓ and the shape exponent β , from the $(\ell, \beta) \leftrightarrow (\bar{k}, \bar{x})$ mapping, where β represents either q or α . However, since the information provided by the theory is limited, it is not possible to infer exactly which particular form of γ governs the dynamics just by measuring (\bar{k}, \bar{x}) of the oscillations. Nevertheless, the characteristic length and compactness of the influence function can be accessed. In the insets of Fig. 7c-d, we show the kernels whose parameters have been extracted from the mapping of each point (\bar{k}, \bar{x}) of Fig. 7a-d. Although one has finite support while the other has (stretched exponential) tails, both present similar coarse-grained appearance for given (\bar{k}, \bar{x}) . In the main frames, we show the oscillations that emerge in each case.

3.4. Two-dimensional landscapes

In this section we show results of simulations for relevant 2D scenarios, verifying that the picture of induced oscillations described up to now for 1D also holds in 2D.

Snapshots of simulations for different 2D landscapes are presented in Fig. 8: a refuge (a), a defect (b), multiple defects (c) and spatial randomness (d) where a wide range of spatial scales are present [27, 18]. It is worth to remark that, in 2D, for the kernel γ_q , patterns only appear in homogeneous landscapes if $q < q_c \simeq 0.25$ (i.e., if $\lambda(k^*) > 0$). Thus, in all the cases of Fig. 8 (using $q = 0.5$) we would not find oscillations if the landscape were homogeneous. In Fig. 8, we see that for 2D the same picture as in 1D is found: decaying oscillations appear near landscape disturbances with a clear wavenumber and decay length. The linear response approach presented in Sec. *Heterogeneous landscapes* can straightforwardly be extended to 2D. Figure 8d shows a case where the landscape is random (in space, but time-independent). This situation, investigated in many previous studies [18, 4], produces a pattern that is noisy but has a dominant wavelength, which is related to ℓ . Furthermore, although there is not a clear identification of decay length from pattern observation, the linear theory would allow to estimate the characteristic spatial correlation length from the width of the spectrum.

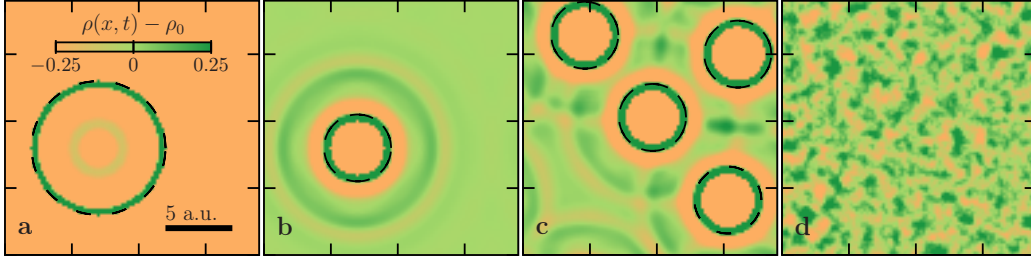


Figure 8: **Long-time spatial distribution in 2D.** Simulated scenarios: (a) a circular region (with radius 5 a.u., highlighted with a black dashed boundary) where the growth rate is positive a (in a strong negative background $a - A$); (b) a circular region (with radius 2.5 a.u., highlighted with a black dashed boundary) where the growth is strongly negative $a - A$ (while outside, it is positive, a); (c) four regions with negative growth rates $a - A$ (in a positive background, a); (d) random landscape with growth rates uniformly distributed in $[0.5a, 1.5a]$. In all cases the interaction kernel is γ_q , with $\ell = 2$ and $q = 0.5$, $D = 10^{-3}$, $a = b = 1$ and $A = 10$. Colors show the deviation from the homogeneous state $\rho(x, t) - \rho_0$ (where $\rho_0 = 1$ for the chosen values of the parameters). For numerical integration, a pseudo-spectral method was used with $\Delta x = 0.2$ and $\Delta t = 10^{-3}$. For details see Ref. [28]

4. Concluding remarks

We have studied the non-local FKPP equation, which is a general modeling of nonlocally competing populations, in the presence of heterogeneous environments. We have identified three types of spatial structures close to a discontinuity of the environment: (i) *sustained oscillations*, (ii) *decaying oscillations*, and (iii) *exponential decay*. We have also shown that these structures, observed through the integration of the population dynamics Eq. (3), can be understood within a theoretical framework, as discussed in Sec. *Semi-infinite habitat*.

In the numerical examples we have chosen to use, as interaction kernel, the family γ_q , because it allows to scan shapes of different compactness. Moreover, results for another important class, the stretched exponential family, are presented in Appendix, showing the same effects. It is worth to remark that, due to computational cost, our numerical study was carried out for 1D, but the same phenomenon also emerges in 2D environments, as shown in Sec. *Two-dimensional landscapes*. The approach developed here can be straightforwardly extended to reach a broader ecological context.

The interesting point is that sharp heterogeneities reveal information on the interaction scales that are otherwise hidden. Then, the natural or artificial interposition of an interface can act as a lens that allows to see what is veiled in a homogeneous landscape. A closer look at this connection is shown in Sec. *Inferring information about the interactions*.

Finally, let us comment that, our choice of sharp interfaces was motivated by the purpose of showing the emergence of essentially three simple classes of structures (i)-(iii) defined above. The single-interface case we analyze is particularly interesting because it puts into evidence the dominant wavenumber and decay length. But this result is actually more general, and can be used to understand the effects of arbitrary heterogeneous landscapes, like the multiple and random cases shown in Fig. 8. It is noteworthy that similar structures emerge behind propagating fronts [4, 29]. Lastly, it is also interesting to remark that the reported results can reach contexts beyond population dynamics, since nonlocality is commonly found in complex systems.

References

- [1] R. Fisher, *Annals of Eugenics* **7**, 355 (1937).
- [2] A. N. Kolmogorov, I. Petrovskii, and N. Piskunov, *Moscow University Mathematics Bulletin* **1**, 1 (1937).
- [3] M. Cencini, C. Lopez, and D. Vergni, *Reaction-Diffusion Systems: Front Propagation and Spatial Structures* (Springer Berlin Heidelberg, Berlin, Heidelberg, 2003), pp. 187–210.
- [4] A. Sasaki, *Journal of Theoretical Biology* **186**, 415 (1997).
- [5] M. A. Fuentes, M. N. Kuperman, and V. M. Kenkre, *Phys. Rev. Lett.* **91**, 158104 (2003).
- [6] E. Hernández-García and C. López, *Phys. Rev. E* **70**, 016216 (2004).
- [7] R. Martínez-García, J. M. Calabrese, E. Hernández-García, and C. López, *Geophysical Research Letters* **40**, 6143 (2013).
- [8] C. E. Tarnita, J. A. Bonachela, E. Sheffer, J. A. Guyton, T. C. Coverdale, R. A. Long, and R. M. Pringle, *Nature* **541**, 398 (2017).

- [9] C. Fernandez-Oto, M. G. Clerc, D. Escaff, and M. Tlidi, *Phys. Rev. Lett.* **110**, 174101 (2013).
- [10] R. Martínez-García, J. M. Calabrese, E. Hernández-García, and C. López, *Phil. Trans. R. Soc. A* **372**, 20140068 (2014).
- [11] J. Liu, R. Martinez-Corral, A. Prindle, D.-y. D. Lee, J. Larkin, M. Gabalda-Sagarra, J. Garcia-Ojalvo, and G. M. Süel, *Science* **356**, 638 (2017).
- [12] T. Bäuerle, A. Fischer, T. Speck, and C. Bechinger, *Nature Communications* **9**, 3232 (2018).
- [13] C. López and E. Hernández-García, *Physica D: Nonlinear Phenomena* **199**, 223 (2004).
- [14] S. Pigolotti, C. López, and E. Hernández-García, *Phys. Rev. Lett.* **98**, 258101 (2007).
- [15] S. Berti, M. Cencini, D. Vergni, and A. Vulpiani, *Phys. Rev. E* **92**, 012722 (2015).
- [16] N. Perry, *Journal of the Royal Society, Interface* **2**, 379 (2005).
- [17] M. G. Turner, R. H. Gardner, R. V. O'Neill, et al., *Landscape ecology in theory and practice* (Springer, 2001).
- [18] L. Ridolfi, P. D'Odorico, and F. Laio, *Noise-Induced Phenomena in the Environmental Sciences* (Cambridge University Press, 2011).
- [19] L. A. da Silva, E. H. Colombo, and C. Anteneodo, *Phys. Rev. E* **90**, 012813 (2014).
- [20] E. H. Colombo and C. Anteneodo, *Phys. Rev. E* **92**, 022714 (2015).
- [21] C. R. Fonseca, R. M. Coutinho, F. Azevedo, J. M. Berbert, G. Corso, and R. A. Kraenkel, *PLOS ONE* **8**, 1 (2013).
- [22] C. Tsallis, *Introduction to nonextensive statistical mechanics: approaching a complex world* (Springer Science & Business Media, 2009).
- [23] E. H. Colombo and C. Anteneodo, *Physical Review E* **86**, 036215 (2012).

- [24] The zeros of $\lambda(k)$ were obtained numerically, by using the Taylor expansion of $\lambda(k)$ around $k = 0$ and solving $Dk^2 + \sum_{n=0}^N \frac{1}{n!} \frac{d^n \tilde{\gamma}}{dk^n} \Big|_{k=0} k^n = 0$, in the limit of sufficiently large N .
- [25] If $k_- < k_+$ are the points at which $\tilde{R}(k_{\pm}) = \tilde{R}(k^*)/2$, then $\Delta k/2 = (k_+ - k_-)/2$. If only k_+ exists then we estimated $\Delta k/2 = k_+ - k^*$.
- [26] E. I. Butikov, *American Journal of Physics* **72**, 469 (2004).
- [27] J. García-Ojalvo and J. Sancho, *Noise in spatially extended systems* (Springer Science & Business Media, 2012).
- [28] R. Montagne, E. Hernández-García, A. Amengual, and M. San Miguel, *Phys. Rev. E* **56**, 151 (1997).
- [29] Y. A. Ganan and D. A. Kessler, *Physical Review E* **97**, 042213 (2018).

Acknowledgements

E.H.C., C.L. and E.H.G. acknowledge financial support from MINECO/AEI/ FEDER through the María de Maeztu Program for Units of Excellence in R&D (MDM- 2017-0711). V.D. and C.A. acknowledge financial support from Coordenação de Aperfeiçoamento de Pessoal de Nível Superior (CAPES), Conselho Nacional de Desenvolvimento Científico e Tecnológico (CNPq), and Fundação de Amparo à Pesquisa do Estado do Rio de Janeiro (FAPERJ).

Appendix A. Results for the stretched exponential kernel

We consider, as a second class of kernels, the stretched exponential family

$$\gamma_{\alpha}(x) = \frac{e^{-|x|/\ell}{}^{\alpha}}{2\ell\Gamma(1 + 1/\alpha)}, \quad (\text{A.1})$$

with $\alpha > 0$ for normalizability. When $\alpha = 1$, it produces the double exponential kernel, whose Fourier transform is $\tilde{\gamma}_1(k) = \frac{1}{1+\ell^2 k^2}$. It includes the Gaussian ($\alpha = 2$), whose Fourier transform is $\tilde{\gamma}_2(k) = e^{-\ell^2 k^2/4}$. And it also reproduces the top-hat kernel in the limit $\alpha \rightarrow \infty$.

In Fig. A.1, we show the growth rate $\lambda(k)$, for three values of α .

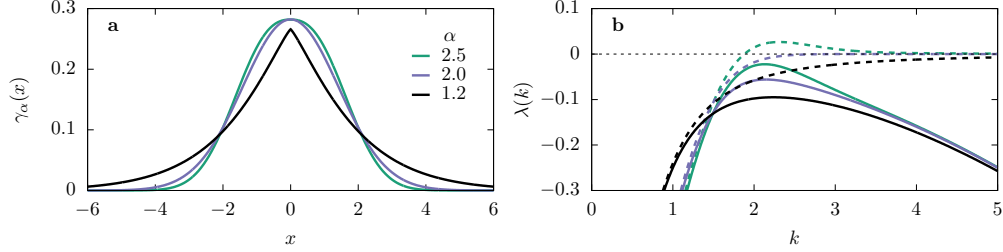


Figure A.1: **Interaction kernel and mode stability in a homogeneous medium.** (a) $\gamma_\alpha(x)$, defined in Eq. (A.1), for the values of α indicated on the figure, and $\ell = 2$. (b) Mode growth rate $\lambda(k)$, for $a = b = 1$, with $D = 0$ (dashed lines) and $D = 10^{-2}$ (solid lines), corresponding to the values of α plotted in (a). The case $\alpha = 2$ is the critical one, for which the maximal value of $\lambda(k)$ at finite k is zero when $D = 0$.

The phase diagram, shown in Fig. A.2a, is qualitatively similar to the corresponding diagram for γ_q , shown in Fig. 5 of the main text. In Fig. A.2b, we characterize the profiles as a function of parameter $2 - \alpha$. Also in this case the behaviors are analogous to those obtained for kernel γ_q .

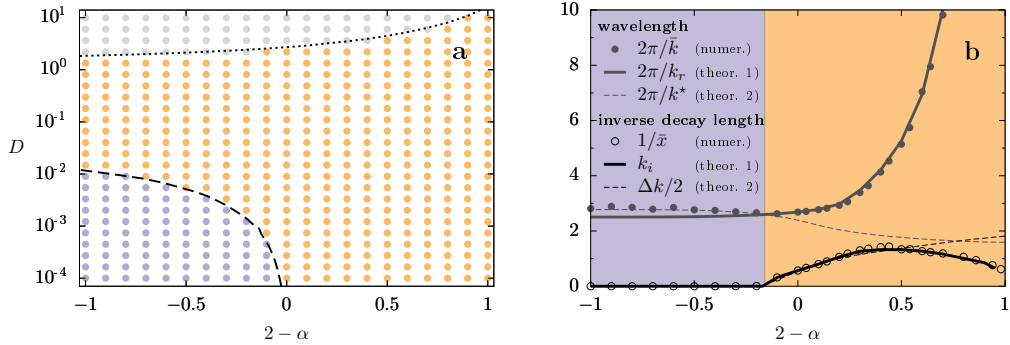


Figure A.2: **Phase diagram and characteristics of the stationary profiles as a function of shape parameter $2 - \alpha$** , for kernel $\gamma_\alpha(x)$ with $\ell = 2$. The remaining conditions and conventions are as in Fig. 5 of the main text.